scientific reports

Check for updates

OPEN

Fragmentation and correlations in a rotating Bose–Einstein condensate undergoing breakup

Sunayana Dutta[1,2]✉, Axel U. J. Lode[3] & Ofir E. Alon[1,2]

The theoretical investigation of rotating Bose–Einstein condensates has mainly focused on the emergence of quantum vortex states and the condensed properties of such systems. In the present work, we concentrate on other facets by examining the impact of rotation on the ground state of weakly interacting bosons confined in anharmonic potentials computed both at the mean-field level and particularly at the many-body level of theory. For the many-body computations, we employ the well-established many-body method known as the multiconfigurational time-dependent Hartree method for bosons. We present how various degrees of fragmentation can be generated following the breakup of the ground state densities in anharmonic traps without ramping up a potential barrier for strong rotations. The breakup of the densities is found to be associated with the acquisition of angular momentum in the condensate due to the rotation. In addition to fragmentation, the presence of many-body correlations is examined by computing the variances of the many-particle position and momentum operators. For strong rotations, the many-body variances become smaller than their mean-field counterparts, and one even finds a scenario with opposite anisotropies of the mean-field and many-body variances. Further, it is observed that for higher discrete symmetric systems of order *k*, namely three-fold and four-fold symmetry, breakup to *k* sub-clouds and emergence of *k*-fold fragmentation take place. All in all, we provide a thorough many-body investigation of how and which correlations build up when a trapped Bose–Einstein condensate breaks up under rotation.

The successful experimental realization of a rotating Bose–Einstein condensate (BEC) has paved the way to explore various rich physics of correlated quantum systems[1–5]. Butts and Rokhsar[6] first evaluated the wave function of a rotating BEC using the lowest Landau level approximation with the help of a Gross-Pitaevskii functional. The rotating ultracold bosonic gases have led to the investigation of the occurrence of quantized vortices[1,3,6], vortex nucleation[7], emergence of quantum fluctuations[8,9], and presence of the fractional quantum Hall effect in weakly interacting quantum systems[10].

There have been studies where breaking up of fast rotating objects is widely detected in systems extending from astronomical objects, e.g., galaxies and supermassive rotating stars[11] to the quantum systems in nuclear physics[12]. In atomic physics, the emergence of superfluid flow of a rotating quantum gas has been explored experimentally in Ref.[13], in an anharmonic potential. Theoretically, the emergence of breakup in a rotating dipolar condensate was investigated in three-dimension in Ref.[14] and finally, in a rotating pancake-like asymmetric quartic-quadratic potential in Ref.[15]. A substantial volume of literature exists corresponding to the rotating BEC, investigating various rich quantum features by employing Gross-Pitaevskii mean-field approximation[16–18]. However, there exists much less studies of rotating BEC in the many-body domain, see[19–24], that explore interesting many-body quantum features like the fragmentation of the condensate and correlations.

Condensation and fragmentation are widely explored many-body features of BEC derived from the properties of the one-body reduced density matrix[25–30]. According to Penrose and Onsager, interacting bosons are said to be condensed if they have a single macroscopic eigenvalue of the one-body reduced density matrix[31], and fragmented if there exist two or more macroscopic eigenvalues[32]. The fragmentation of condensates has been thoroughly studied for non-rotating systems[29,30,33–47]. However, these many-body features have relatively been less extensively investigated in the rotating frame[7,48–50].

In the regime of "ultrafast rotation", when the rotation frequency comes closer to the trapping frequency in case of a harmonic trapping potential, the system would tend to escape as the centrifugal force would cancel the trapping force. This problem can be resolved either by introducing an anharmonic term into the confining

[1]Department of Physics, University of Haifa, 3498838 Haifa, Israel. [2]Haifa Research Center for Theoretical Physics and Astrophysics, University of Haifa, 3498838 Haifa, Israel. [3]Institute of Physics, Albert-Ludwig University of Freiburg, Hermann-Herder-Strasse 3, 79104 Freiburg, Germany. ✉email: sdutta@campus.haifa.ac.il

potential or by adding anisotropy in the harmonic potential. Anisotropy makes the confining potential elongated. Ref.[51] investigated the appearance of vortex rows of BEC in an anisotropic potential under rotation using Gross-Pitaevskii formalism. Motivated by these findings, in this work, we study a system of bosons subject to rotation confined in various anharmonic trap geometries with discrete rotational symmetry in two-dimension 2D, namely an elongated trap, a three-fold symmetric trap and finally four-fold symmetric trap.

There exist several ideas to induce mechanical rotation and coupling of the internal states in the condensate, such as, phase imprinting (using an electromagnetic field) as proposed by Williams and Holland in Ref.[52] and optical spoon stirring method where quantized vortices are observed in a stirred gaseous condensate of atomic rubidium[1]. Here, we study the physics of a 2D weakly interacting ultracold bosons confined in different anharmonic potentials both at the mean-field level and particularly at the many-body level of theory. Specifically, we investigate how the system transformed from a fully-condensed state into a fragmented state followed by breaking up of the condensate density induced by the rotational motion. As variance is a sensitive probe that characterizes many-body correlations even for fully condensed systems[53,54], hence we also analyze the variances of many-particle operators of the fragmented state in the rotating frame. The qualitative difference between the mean-field and many-body variances is a useful tool to explain the nature of many-body correlations. The many-particle position variance characterizes to what extent a wave-packet spreads or narrows down, similarly the momentum variance is associated with the size of the wave-packet in momentum space. Hence, we emphasize on the emergence of correlations by investigating variances of many-particle operators like the position, momentum and angular momentum. Interestingly, the fluctuations present in the system are hardly observed in the angular momentum variance. Thus, we only present the position and momentum variances in the main text and give the detail discussion of the angular momentum variance in the supplemental material.

The time-dependent Gross-Pitaevskii mean-field theory[55,56] is the most celebrated theoretical model to investigate the many-particle systems of ultracold bosonic atoms. However, this method is unable to study fragmentation and correlations owing to its building via the mean-field ansatz. In this paper, we employ a well established many-body numerical method named the multiconfigurational time-dependent Hartree method for bosons (MCTDHB)[57,58] to accurately solve the Schrödinger equation at the many-body level for ultracold atoms subject to a rotation. The MCTDHB method is a bosonic version of the MCTDH family of methods[59–74] which is able to self-consistently describe the physics involving the presence of many-body correlations. The main focus of the applications of MCTDHB has been the emergence of fragmentation of the condensate, where the one-body reduced density matrix has multiple significant eigenvalues. For numerical simulation of the results presented in this work, we use the MCTDH-X software[74–77]. Finally, the supplemental material reports the benchmarking of MCTDHB for an exactly solvable many-body model under rotation and also presents the convergence of the many-body results of our present work.

Setup and theoretical tools

We consider a system of weakly interacting bosonic atoms in two spatial dimensions 2D confined in non-spherically symmetric trapping potentials in the rotating frame. The properties of these trapped bosons can be described by the (time-dependent) many-body Schrödinger equation. The Schrödinger equation dealing with a many-boson system is usually solved by employing the mean-field Gross-Pitaevskii approximation. However, the reduced density matrix involved in the Gross-Pitaevskii approximation has only a single eigenvalue and it involves a single basis state and thereby is unable to capture the many-body features such as fragmentation and correlations.

In MCTDHB, the (time-dependent) optimized one-body basis is used. Here the basis set and the expansion coefficients in the basis are optimized variationally[57,58]. The MCTDHB is a numerically exact method[78] and can describe both coherent and fragmented condensates. MCTDHB includes the theory of Gross-Pitaevskii approximation as a special case when only a single one-body state is considered.

Hamiltonian. The general Hamiltonian of N interacting bosons is given as

$$\hat{H} = \sum_{j=1}^{N} \hat{h}(\mathbf{r}_j) + \sum_{j<k} \hat{W}(\mathbf{r}_j - \mathbf{r}_k), \tag{1}$$

where the single-particle Hamiltonian

$$\hat{h}(\mathbf{r}) = \hat{T}(\mathbf{r}) + \hat{V}(\mathbf{r}) \tag{2}$$

is composed of the kinetic energy and the external potential energy, respectively. Here, the interaction of ultracold dilute bosonic gases is considered to be a finite range interaction and modelled by a Gaussian function[65,66,79], $\hat{W}(\mathbf{r}-\mathbf{r}') = \frac{\lambda_0}{2\pi\sigma^2} e^{-\frac{(\mathbf{r}-\mathbf{r}')^2}{2\sigma^2}}$ with $\sigma = 0.25$. This avoids the regularization of the delta contact potential in 2D. The interaction strength λ_0 is scaled with the number of bosons N as $\Lambda = \lambda_0(N-1)$, where Λ is the interaction parameter. One uses the interaction parameter to define the mean-field regime. In our study, we work in the units $\hbar = m = 1$ and all the quantities are dimensionless. We also consider three different trapping potentials $\hat{V}(\mathbf{r})$ that we shall discuss in the next section. The first setup is the elongated trap − that leads to breaking up of the ground state density into two clouds. After that we move to more complex traps, namely three-fold symmetric and four-fold symmetric traps to investigate and establish the generality of the results. Hence, our strategy is to first study an elongated trap, and then a three-fold symmetric trap, and finally, a four-fold symmetric trap to see what stays between the two to three and the three to four-fold symmetric traps.

In the rotating frame, the kinetic energy operator is modified and can be written as,

$$\hat{T}(\mathbf{r}) = \frac{1}{2}(\hat{p}_x^2 + \hat{p}_y^2) - \omega_r \hat{l}_z, \tag{3}$$

here ω_r is the rotation frequency and $\hat{l}_z = \hat{x}\hat{p}_y - \hat{y}\hat{p}_x$ is the angular-momentum operator.

An alternative way to mimic the rotational effect in the condensate is by introducing a synthetic gauge field $\mathbf{A}(\mathbf{r})$ as

$$\hat{T}(\mathbf{r}) = \frac{1}{2}\left[-i\nabla_{\mathbf{r}} - q\mathbf{A}(\mathbf{r})\right]^2. \tag{4}$$

Consider the following general form of the gauge field:

$$\mathbf{A}(\mathbf{r}) = (ay, bx, 0). \tag{5}$$

Then, expansion of Eq. (4) leads to,

$$\hat{T}(\mathbf{r}) = \frac{1}{2}(\hat{p}_x - ay)^2 + \frac{1}{2}(\hat{p}_y - bx)^2 = \frac{1}{2}(\hat{p}_x^2 + \hat{p}_y^2) - (\hat{p}_x ay + \hat{p}_y bx) + \frac{1}{2}(a^2y^2 + b^2x^2). \tag{6}$$

For the specific case $b = -a$, Eq. (6) becomes

$$\hat{T}(\mathbf{r}) = \frac{1}{2}(\hat{p}_x^2 + \hat{p}_y^2) - a\hat{l}_z + \frac{1}{2}a^2(y^2 + x^2). \tag{7}$$

Combining Eqs. (2), (3) and (7) we have

$$\hat{h}(\mathbf{r}) = \hat{T}(\mathbf{r}) + \hat{V}'(\mathbf{r}), \tag{8}$$

where the modified confining potential is $\hat{V}'(\mathbf{r}) = \hat{V}(\mathbf{r}) + \frac{1}{2}a^2\mathbf{r}^2$ and $a = \omega_r$ corresponds to the rotation frequency of the condensate.

Many-body method. The MCTDHB method employs time-adaptive orbitals to represent the field operator as a sum of the M time-dependent single-particle states

$$\hat{\Psi}(\mathbf{r}, t) = \sum_{j=1}^{M} \hat{b}_j \phi_j(\mathbf{r}, t). \tag{9}$$

The ansatz of the MCTDHB wavefunction is

$$|\Psi(t)\rangle = \sum_{\vec{n}} C_{\vec{n}} |\vec{n}, t\rangle. \tag{10}$$

The summation in Eq. (10) runs over all $\binom{N+M-1}{N}$ possible time-dependent configurations $\vec{n} = (n_1, \ldots, n_M)$ with fixed particle number $N = \sum_{i=1}^{M} n_i$. To derive the MCTDHB equations, the time-dependent variational principle[80–82] is employed for the ansatz in Eq. (10). Thus, in Lagrangian formulation, the functional action of the time-dependent Schrödinger equation with many-body ansatz, Eq. (10) can be written as[57,58],

$$S[\{C_{\vec{n}}(t)\}, \{\phi_j(\mathbf{r}, t)\}] = \int dt \{\langle\Psi|\hat{H} - i\frac{\partial}{\partial t}|\Psi\rangle - \sum_{j,k=1}^{M} \mu_{jk}(t)[\langle\phi_j|\phi_k\rangle - \delta_{jk}]\}, \tag{11}$$

where $\mu_{jk}(t)$ is the time-dependent Lagrange multipliers and is introduced to ensure that the time-dependent orbitals remain orthonormal during propagation. Thus, resulting in two-coupled equations of motion – a set of linear equations for the coefficients $\{C_{\vec{n}}\}$

$$H_{\vec{n}\vec{n}'}(t) C_{\vec{n}}(t) = i\frac{\partial C_{\vec{n}}(t)}{\partial t}, \tag{12}$$

where the matrix $H_{\vec{n}\vec{n}'} = \langle\vec{n}; t|\hat{H}|\vec{n}'; t\rangle$ is time-dependent and a set of non-linear equations for the orbitals $\{\phi_j(\mathbf{r}); j = 1, \ldots, M\}$,

$$i|\phi_j\rangle = \hat{\mathbf{P}}\left[\hat{h}|\phi_j\rangle + \sum_{k,s,q,l=1}^{M} \{\rho(t)\}_{jk}^{-1} \rho_{ksql} \hat{W}_{sl} |\phi_q\rangle\right], \tag{13}$$

where $\hat{\mathbf{P}} = 1 - \sum_{j'=1}^{M} |\phi_j'\rangle\langle\phi_j'|$ is the projection operator, $\rho_{jk} = \langle\Psi|\hat{a}_j^\dagger \hat{a}_k|\Psi\rangle$ and $\rho_{ksql} = \langle\Psi|\hat{a}_k^\dagger \hat{a}_s^\dagger \hat{a}_q \hat{a}_l|\Psi\rangle$ are the matrix elements of the one-body and two-body RDMs. $\hat{w}_{sl} = \int d\mathbf{r}' \hat{\phi}_s^*(\mathbf{r}'; t) \hat{W}(\mathbf{r} - \mathbf{r}') \hat{\phi}_l(\mathbf{r}; t)$ is the matrix elements of the two-body interaction potential, see Refs.[57,58] for details and derivation of the equations of motion. In the following work, the self-consistent ground state is achieved by relaxing the system via imaginary-time

propagation and is hence determined by the variational principle. Thus, in the following sections, we omit the time-dependency from the various quantities and observables that are involved in the many-body simulations.

Quantities of interest. In this section, we define the quantities of interest, namely the one-body density, the eigenvalues of the one-body reduced density matrix (RDM), the expectation value of the angular momentum operator, and finally, the many-particle variances of the position, momentum, and angular momentum operators.

One-body reduced density matrix (RDM), one-body density, and natural occupations. The one-body RDM of the N-boson state $|\Psi\rangle$ is a hermitian matrix and is defined as

$$\rho^{(1)}(\mathbf{r},\mathbf{r}') = \langle\Psi|\hat{\Psi}^\dagger(\mathbf{r}')\hat{\Psi}(\mathbf{r})|\Psi\rangle = \sum_{k,q}\rho_{kq}\phi_k^*(\mathbf{r}')\phi_q(\mathbf{r}) \tag{14}$$

in its eigenbasis $\{\phi_q(\mathbf{r})\}$. The matrix elements $\rho_{kq} = \langle\Psi|\hat{b}_k^\dagger\hat{b}_q|\Psi\rangle$ represent the one-body RDM using M orbitals corresponding to the creation (annihilation) operators $\hat{b}_k^\dagger$ ($\hat{b}_q$). The diagonal of $\rho^{(1)}(\mathbf{r},\mathbf{r}')$ is referred to as the one-body density $\rho(\mathbf{r})$ which is $\rho(\mathbf{r}) = \rho^{(1)}(\mathbf{r},\mathbf{r}'=\mathbf{r})$.

The eigenvalues of the one-body RDM are obtained by the diagonalization of Eq. (14) which corresponds to a unitary transformation of the orbitals $\phi_q(\mathbf{r})$ to the natural orbitals $\phi_j^{(NO)}(\mathbf{r})$ as

$$\frac{\rho^{(1)}(\mathbf{r},\mathbf{r}')}{N} = \sum_j n_j\phi_j^{(NO),*}(\mathbf{r}')\phi_j^{(NO)}(\mathbf{r}). \tag{15}$$

Here, the eigenvalues n_j are normalized as $\sum_{j=1}^M n_j = 1$ and, without loss of generality, they are sorted in magnitude such that $n_1 \geq n_2 \geq \ldots$ throughout this work. The eigenvalues n_j are termed natural occupations and characterize the degree of condensation and fragmentation of the bosons. Thus, the system with one-body RDM consisting only a single macroscopically-contributing eigenvalue n_1 is said to be condensed[31]. When the one-body RDM has k macroscopically-occupied eigenvalues, the system is referred to as k-fold fragmented[34].

Angular momentum. For a 2D many-particle systems, there is only a single component of the angular momentum operator, i.e.,

$$\hat{L}_Z = \sum_{j=1}^N \hat{l}_{z_j} = \sum_{j=1}^N \frac{1}{i}\left(\hat{x}_j\frac{\partial}{\partial y_j} - \hat{y}_j\frac{\partial}{\partial x_j}\right). \tag{16}$$

Bosonic systems with angular momentum provide rich quantum features beyond mean-field theory, such as, phantom vortices[83], spatially partitioned vortices[53], and fragmentation[53,83,84]. In the following studies, we investigate the expectation value of the angular momentum operator per particle $\frac{1}{N}\langle\Psi|\hat{L}_Z|\Psi\rangle$, for three different confining traps to see the effect of the rotation. In our system, we expect an intricate dynamics of the angular momentum acquisition under rotation and build up of correlations.

Many-particle variances. The variance of a many-particle observable $\hat{O} = \sum_{j=1}^N \hat{o}(\mathbf{r}_j)$ can be written as[85]

$$\begin{aligned}\frac{1}{N}\Delta^2_{\hat{O}} =& \frac{1}{N}\left[\langle\Psi|\hat{O}^2|\Psi\rangle - \langle\Psi|\hat{O}|\Psi\rangle^2\right] = \\ =& \frac{1}{N}\left\{\sum_j n_j\int \mathrm{d}\mathbf{r}\,\phi_j^{*(NO)}(\mathbf{r})\hat{o}^2\phi_j^{(NO)}(\mathbf{r}) - \left[\sum_j n_j\int \mathrm{d}\mathbf{r}\,\phi_j^{*(NO)}(\mathbf{r})\hat{o}\phi_j^{(NO)}(\mathbf{r})\right]^2 + \right. \\ &\left. + \sum_{jklm}\rho_{jklm}\left[\int \mathrm{d}\mathbf{r}\phi_j^{*(NO)}(\mathbf{r})\hat{o}\phi_l^{(NO)}(\mathbf{r})\right]\left[\int \mathrm{d}\mathbf{r}\phi_k^{*(NO)}(\mathbf{r})\hat{o}\phi_m^{(NO)}(\mathbf{r})\right]\right\}.\end{aligned} \tag{17}$$

Here, the expectation value of $\hat{O} = \sum_{j=1}^N \hat{o}(\mathbf{r}_j)$ is dependent only on the one-body operator, whereas the expectation of $\hat{O}^2$ is a combination of one- and two-body operators $\hat{O}^2 = \sum_{i=1}^N \hat{o}^2(\mathbf{r}_j) + \sum_{j<k} 2\hat{o}(\mathbf{r}_j)\hat{o}(\mathbf{r}_k)$. ρ_{jklm} are the two-particle reduced density matrix elements, $\rho(\mathbf{r}_1,\mathbf{r}_2,\mathbf{r}_1',\mathbf{r}_2') = \sum_{jklm}\rho_{jklm}\phi_j^*(\mathbf{r})\phi_k^*(\mathbf{r})\phi_l(\mathbf{r})\phi_m(\mathbf{r})$. In the following work, to analyze the emergence of many-body correlations in the rotating condensate, we study the many-particle variances per particle of the position, momentum, and angular momentum operators[54].

Many-body physics of Bose–Einstein condensates breaking up under rotation: results and discussion

We investigate the impact of rotation on the ground state of weakly interacting bosonic atoms by dividing the analysis into two main parts depending on the confining anharmonic potentials. First, the breakup and fragmentation processes in an elongated trap are investigated and then the breakup and fragmentation in more complicated traps of discrete spatial symmetry are explored. In the following sections, we analyze the effect of rotation

on various static properties, namely the ground state energy, one-body density, natural occupations, expectation value of the angular momentum operator, and finally, the variances of the many-particle position, momentum, and angular momentum operators as a function of the rotation frequency ω_r. For the numerical computations, the MCTDH-X implementation of the MCTDHB theory is employed[74–77]. In our work, we consider $N = 10$ weakly interacting ultracold bosonic atoms interacting via a Gaussian interaction[65,66,79] with the interaction parameter chosen as $\Lambda = 0.1$ throughout the computations. The grid used to represent the Hamiltonian Equation (1), see section "Hamiltonian", extends from $[-8, 8)$ to $[-8, 8)$ and comprises of 128×128 discrete variable representation (exponential) functions to represent each of the orbitals $\phi_j(\mathbf{r})$.

Breaking up to two clouds and pathway to two-fold fragmentation. Let us discuss the impact of rotation on the weakly interacting bosons trapped in an elongated confinement. The elongated trap is an anharmonic potential that elongates the condensate in the x-direction and can be written as

$$V(\mathbf{r}) = \frac{1}{4}(0.8x^2 + y^2)^2. \tag{18}$$

For this trap, we consider $M = 4$ self-consistent orbitals to investigate the ground state properties of the condensate. We recomputed these results with $M = 8$ self-consistent orbitals to check the convergence of the system, see the elaborate discussion in the supplemental material. The rotation frequency range is $\omega_r = [0, 2.0]$ in this trap.

Figure 1 shows the behaviour of the ground-state energy per particle E/N, in the rotating frame computed both at the mean-field and many-body levels. Initially, E/N remains almost constant for slow rotation. Then, E/N drops gradually with further increase in ω_r as evident from Fig. 1. It is also observed that the energies computed both at the mean-field and many-body levels practically coincide each other for all ω_r. The inset of Fig. 1 corresponds to the energy difference per particle $\Delta E/N$, between the mean-field and many-body energies defined as $\Delta E = E_{MF} - E_{MB}$. The energy difference remains minimum till about $\omega_r = 1.2$. Subsequently, $\Delta E/N$ exhibits some structures for an intermediate range of ω_r around $\omega_r \sim 1.3$. Finally, the energy difference slightly rises from of the order of 10^{-5} to 10^{-3} for larger rotation frequencies $\omega_r \geq 1.6$. The presence of these structures at the intermediate rotation might suggest that something interesting is happening at the many-body level. Therefore, we dig deeper than the energy of the system to see the many-body features.

Now let us discuss the behaviour of the ground-state densities per particle $\frac{\rho(\mathbf{r})}{N}$ of the rotating condensate confined in the elongated trap. The densities computed at the many-body level of theory are shown for three different rotation frequencies ω_r in Fig. 2. In absence of rotation, the density displays a single cloud where all bosons accumulate in the center of the trap. This behaviour persists with the inclusion of rotation for slow rotation frequencies, e.g., at $\omega_r = 0.5$. Further increase in rotation induces a breaking of the density into two clouds. The breakup of the ground-state density confined in the potential given by Eq. (18) corresponds to the scenario where the minimum of the potential is splitted into two parts and shifted with rotation by creating an effective double-well potential. It is also observed that the distance between the two densities increases with increase of ω_r [Fig. 2b, c]. We have also computed the density per particle at the mean-field level and identical features are observed in the density profile. Hence, it is observed that the densities computed at the mean-field and many-body levels in the real space show identical pattern. In the density profile, we show three specific frequencies that correspond to slow, fast, and faster rotations.

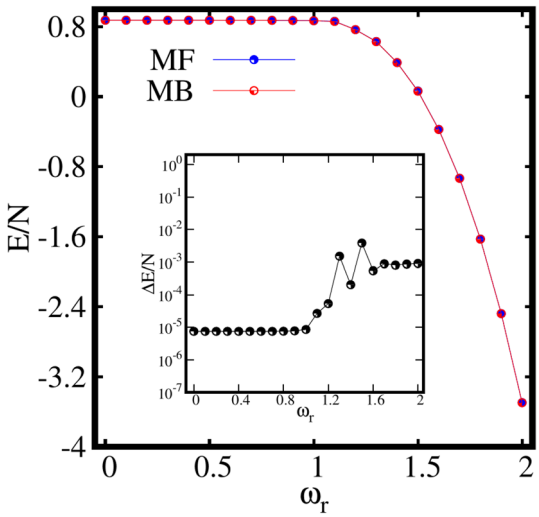

Figure 1. Behaviour of the ground state energy per particle E/N as a function of the rotation frequency ω_r in an elongated trap computed at the mean-field (MF) and many-body (MB) levels (with M=1 and M=4 self-consistent orbitals, respectively). The inset shows the energy difference between the mean-field and many-body energies. All quantities shown are dimensionless.

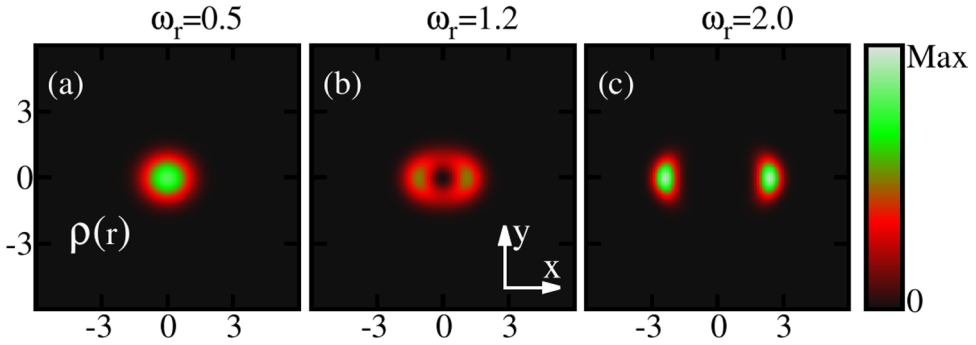

Figure 2. The one-body densities per particle are shown for three different rotation frequencies ω_r in the elongated trap at the many-body level. M=4 self-consistent orbitals are used. The density computed at the mean-field (not shown) and many-body levels depict identical features for almost all ω_r, see the supplemental material, Sec. S6, for further discussion. All quantities shown are dimensionless.

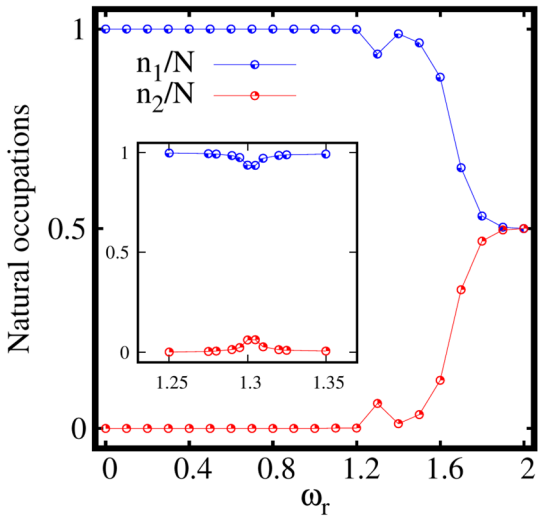

Figure 3. Pathway from condensation to fragmentation in the rotating elongated trap. Two-fold fragmentation is observed with increase in rotation. The two leading natural occupations n_1/N and n_2/N, are shown as a function of the rotation frequency ω_r. $M = 4$ self-consistent orbitals are used. The third and fourth natural occupations satisfy $n_3/N, n_4/N \leq 10^{-5}$, see the supplemental material. All quantities shown are dimensionless.

To understand whether the splitting of the density into two clouds [as shown in Fig. 2c] for faster rotations leads to fragmentation of the condensate, we further discuss the dependence of the natural occupations $\frac{n_j}{N}$. In the elongated trap, four natural occupations corresponding to the four natural orbitals are employed and found to vary with the rotation frequency ω_r (see Fig. 3).

The system remains fully condensed, i.e., $\frac{n_1}{N} \sim 1$, $\frac{n_2}{N} \sim \frac{n_3}{N} \sim \frac{n_4}{N} \leq 10^{-5}$ with the inclusion of rotation till about $\omega_r = 1.1$ [see Fig. S2a of the supplemental material, which displays the depletion as a function ω_r on a log scale]. As ω_r increases further, the first natural occupation number n_1/N, falls of gradually following an increase in population of the second natural occupation number n_2/N. The other two natural occupation numbers remain almost the same as $\frac{n_3}{N} \sim \frac{n_4}{N} \leq 10^{-5}$. For faster rotation at $\omega_r = 2$, the state becomes essentially fully two-fold fragmented with natural occupations of $\frac{n_1}{N} \approx \frac{n_2}{N} \approx 50\%$. This signifies equally populated two leading natural orbitals, whereas $\frac{n_3}{N}$ and $\frac{n_4}{N}$ remain essentially unpopulated. For an intermediate frequency, $\omega_r = 1.3$, we observe a scenario where n_1 shows a deep followed by a peak in n_2. To understand this feature, we zoom in at the intermediate points between the rotation frequencies $\omega_r = 1.2$ and $\omega_r = 1.4$ as shown in the inset of Fig. 3. A smooth transition is found, from coherence via loss of coherence to build up of coherence. This transition might suggest the presence of a resonant-like behaviour of the interacting bosons in the elongated 2D trap at this specific rotation frequency.

To intermediately summarize, for weakly interacting bosons confined in an elongated trap [Eq. (18)], inclusion of rotation triggers a transition from a fully condensed state to a fully two-fold fragmented state with equally populated two leading natural orbitals. Thus, it can be concluded that the rotation can be used as a tool to manipulate fragmentation.

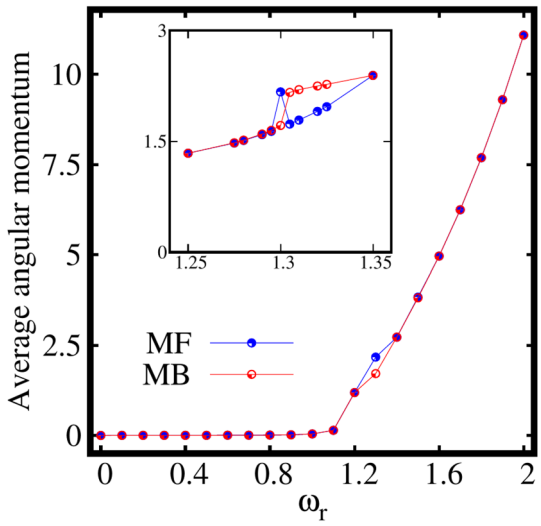

Figure 4. Expectation value of angular momentum operator $\langle \hat{L}_Z \rangle / N$, computed at the mean-field (MF) and many-body (MB) levels [with $M = 1$ and $M = 4$ self-consistent orbitals, respectively] as a function of the rotation frequency ω_r for the elongated trap. Actual data are points. The continuous curves are only to guide the eye. All quantities shown are dimensionless.

Next, let us discuss the behaviour of the expectation value of the angular momentum per particle $\frac{\langle \psi | \hat{L}_Z | \psi \rangle}{N}$, computed at the mean-field and many-body levels as a function of the rotation frequency ω_r. It is observed from Fig. 4 that the mean-field and many-body angular momenta exactly coincide each other at all ω_r except for the intermediate rotation frequency around $\omega_r = 1.3$ [see the inset of Fig. 4], the resonance regime. The following features can be concluded from the behaviour of angular momentum in the resonance regime,

(1) The resonance behaviour is evident both in the mean-field and many-body momenta.
(2) The mean-field resonance regime has a narrow peak, however the many-body resonance has a wider width.
(3) The mean-field resonance starts slightly earlier than the many-body resonance.
(4) At the resonance frequency, the condensate absorbs significant angular momentum.

These resonance features are discussed elaborately in the supplemental material, see Sec. S6. The angular momentum remains minimum till about $\omega_r = 1.1$. For $\omega_r = 1.2$ (the rotation frequency that corresponds to the breakup of the density), the rotation generates a state where significant angular momentum enters the system with $\langle \hat{L}_Z \rangle / N > 1$. The angular momentum of the condensate gradually increases with further increase of the rotation.

As we know, the variance is a sensitive probe of correlations that allows one to study the quantum fluctuations present in a system[53,54]. Thus, it would be interesting to investigate the variance of many-particle operators which signifies many-body correlations for the fragmented condensate in the rotating frame. Therefore, we further analyze the impact of rotation on the behaviour of the many-particle variances of position and momentum operators which are sensitive to rotation.

Fig. 5a, b display the behaviour of the many-particle position variance per particle $\frac{1}{N}\Delta^2_{\hat{X},\hat{Y}}$ along the x and y-directions respectively, as a function of the rotation frequency ω_r in the elongated trap. The mean-field and many-body position variances along the x- direction $\frac{1}{N}\Delta^2_{\hat{X}}$, coincide till about $\omega_r = 0.9$, indicating the essential absence of correlations in the system [Fig. 5a]. Further, the mean-field position variance monotonically increases with ω_r which signifies spreading of the density as observed in Fig. 2. Also, the many-body position variance slowly increases till $\omega_r = 1.2$. But, now, we observe a deep at $\omega_r = 1.3$ that corresponds to the resonance regime as appeared in the natural occupations and the angular mometum figures, see insets of Figs. 3 and 4. We will discuss more about this regime later in this section. After increasing and reaching a maximum at rotation frequency of about $\omega_r \sim 1.4$, $\frac{1}{N}\Delta^2_{\hat{X}}$ starts to decrease which incorporates the emergence of a small amount of depletion of the condensate [see Fig. 5a]. For a faster rotation, at $\omega_r = 2$, the position variance $\frac{1}{N}\Delta^2_{\hat{X}}$ decreases significantly which goes hand in hand with the emergence of fragmentation of the condensate. Similar behaviour of the position variance along the x-direction is observed in a two-dimensional double well in[86], albeit without the resonant-like behaviour described above. The position variance per particle along the y-direction $\frac{1}{N}\Delta^2_{\hat{Y}}$ is almost frozen and varies slowly as shown in Fig. 5b. This might suggest that excitations along the tighter y-directions are practically not involved, at least as far as the position variance is considered. The $\frac{1}{N}\Delta^2_{\hat{Y}}$ computed at the mean-field level matches that at the many-body level almost for all the rotation frequencies except of small difference for the intermediate ω_r. As above, convergence of the results is detailed in the supplemental material.

Further, we can describe the anisotropy of the variance by considering two facts,

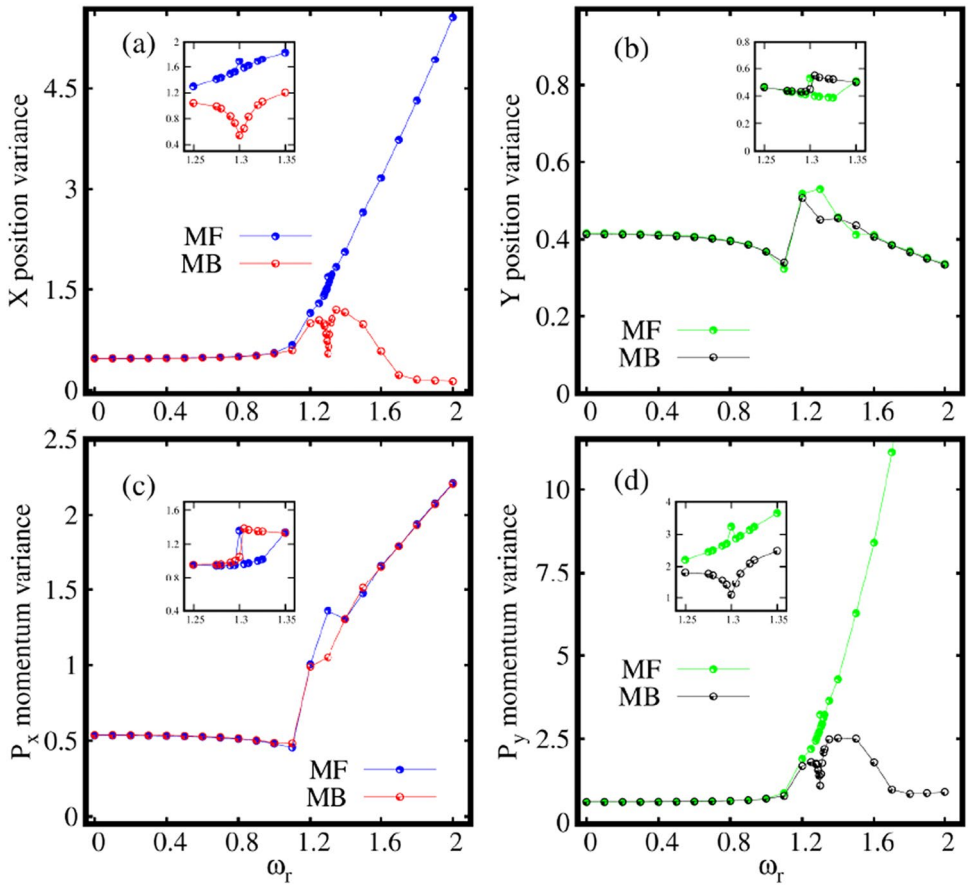

Figure 5. Dependence of the the many-particle position and momentum variances on the rotation in the elongated trap. Shown are (**a**) $\frac{1}{N}\Delta^2_{\hat{X}}$, (**b**) $\frac{1}{N}\Delta^2_{\hat{Y}}$, (**c**) $\frac{1}{N}\Delta^2_{\hat{P}_X}$, and (**d**) $\frac{1}{N}\Delta^2_{\hat{P}_Y}$ as a function of ω_r at the many-body level (MB) [$M = 4$ self-consistent orbitals] and at the mean-field level (MF) [$M = 1$ self-consistent orbital]. All quantities shown are dimensionless.

(1) by comparing two quantities, one along the x- direction and the other along the y- direction, whether they are similar or different.

(2) by comparing these quantities at the mean-field and many-body levels which demonstrates whether the anisotropy of the many-particle variances are alike or opposite. Hence, in the elongated trap and for small rotations, it is observed that

$$\frac{1}{N}\Delta^2_{\hat{X}}|_{MB} < \frac{1}{N}\Delta^2_{\hat{Y}}|_{MB}, \text{ at MB}$$
$$\frac{1}{N}\Delta^2_{\hat{X}}|_{MF} < \frac{1}{N}\Delta^2_{\hat{Y}}|_{MF}, \text{ at MF.}$$

Thus, the anisotropy of the many-particle position variance computed at the mean-field and many-body levels are alike at slow rotation. However, for fast rotation we find

$$\frac{1}{N}\Delta^2_{\hat{X}}|_{MB} < \frac{1}{N}\Delta^2_{\hat{Y}}|_{MB}, \text{ at MB}$$
$$\frac{1}{N}\Delta^2_{\hat{X}}|_{MF} > \frac{1}{N}\Delta^2_{\hat{Y}}|_{MF}, \text{ at MF.}$$

Hence, it indicates that the many-particle position variances display opposite anisotropy when computed at the mean-field and many-body levels.

Now, we investigate the behaviour of the many-particle momentum variance per particle $\frac{1}{N}\Delta^2_{\hat{P}_X,\hat{P}_Y}$ along the x- and y-directions as a function of rotation frequency ω_r in the elongated trap [Fig. 5c, d]. It is observed that unlike the position variance, the mean-field and many-body momentum variances along the x-direction are almost similar, see Fig. 5c. The momentum variances computed at the mean-field and many-body levels gradually increase from $\omega_r = 1.2$ onwards. This corroborates the narrowing of the density lobes along the x-direction in real space. The momentum variance in the y-direction displays a completely different picture, see Fig. 5d. The mean-field and many-body variances match each other till $\omega_r = 1.1$. However, for a faster rotation, the

momentum variance computed at the mean-field deviates from that computed at the many-body level in the y-direction. $\frac{1}{N}\Delta^2_{\hat{P}_Y}$ displays similar behaviour as the $\frac{1}{N}\Delta^2_{\hat{X}}$ as clear from Fig. 5a. Thus, excitations along the y-direction plays a role in the momentum space as a result of rotation.

Inverse to the position variance, in the case of the momentum variance for slow rotation we find

$$\frac{1}{N}\Delta^2_{\hat{P}_X}|_{MB} > \frac{1}{N}\Delta^2_{\hat{P}_Y}|_{MB}, \text{ at MB}$$
$$\frac{1}{N}\Delta^2_{\hat{P}_X}|_{MF} > \frac{1}{N}\Delta^2_{\hat{P}_Y}|_{MF}, \text{ at MF.}$$

Hence, the anistropy of the momentum variances are alike when computed at the many-body and mean-field levels of theory for slow rotation. For a faster rotation however, we find

$$\frac{1}{N}\Delta^2_{\hat{P}_X}|_{MB} > \frac{1}{N}\Delta^2_{\hat{P}_Y}|_{MB}, \text{ at MB}$$
$$\frac{1}{N}\Delta^2_{\hat{P}_X}|_{MF} < \frac{1}{N}\Delta^2_{\hat{P}_Y}|_{MF}, \text{ at MF.}$$

This signifies the presence of opposite anisotropy of the momentum variance. This feature was not found before for static double well[86]. Hence, this indicates one of the distinct features of the rotation, which makes both the many-particle position and momentum variances show opposite anisotropies with respect to the mean-field and many-body levels in the elongated trap. The rotation localized the position variance in the long direction and the momentum variance in the narrow direction and this is purely a many-body effect. Further, in the resonance regime as dicussed above (around $\omega_r = 1.3$), we observe the following distinct features in the quantum correlations,

(1) The resonance behaviour is evident both in the mean-field and many-body fluctuations.
(2) The mean-field resonance regime has a narrow peak, however the many-body resonance has a wider width.
(3) The mean-field resonance starts slightly earlier than the many-body resonance.
(4) The mean-field and many-body resonances are in the opposite direction for the X position [Fig. 5a] and P_y momentum variances [Fig. 5d] which are sensitive to depletion in the condensate. However, for the Y position [Fig. 5b] and P_x momentum variances [Fig. 5c], the mean-field and many-body resonances are oriented in the same direction.

We explain these resonance features more elaborately in the supplemental material, see Sec. S6 for further discussion.

Let us briefly summarize the results so far. The ground state of a Bose–Einstein condensate in a two-dimensional elongated trap is analyzed in presence of rotation. Here, the ground state density splits into two clouds for fast rotation. It is fascinating to observe the effect of rotation on the condensate as it leads to a transition from condensed state to a fully two-fold fragmented state in a single well without ramping up a barrier. Thus, rotation can be used as a probe to manipulate various degrees of fragmentation which we will further discuss in the next section where higher-order fragmentations are explored. Further, we observe the presence of an opposite anisotropy both in the position and momentum variances by comparing the mean-field and many-body results for fast rotations.

Breaking up to several clouds and pathway to higher-order fragmentation. So far in the elongated trap, we observe breaking up of the ground state density into two clouds, followed by the emergence of two-fold fragmentation and presence of opposite anisotropy both in the position and momentum variances for faster rotations. Now, it would be fascinating to explore some more complex potentials with k-fold rotational symmetry, explicitly three-fold and four-fold symmetric potentials, to analyze the impact of rotation on generic properties. Would the density break into more than two clouds? Is higher-order fragmentation possible? How would the angular momentum enter into the condensate? Finally, when correlations set in, who wins, the many-body or the mean-field variance? Both for the position and momentum variances?

Bosons in a three-fold symmetric trap under rotation. In this section, we analyze the impact of rotation on weakly interacting bosons confined in a three-fold symmetric trap of the form

$$V(\mathbf{r}) = \frac{1}{5}(x^2+y^2)^2 + \frac{1}{5}(x^2y - \frac{1}{3}y^3). \tag{19}$$

In this trap, we consider $M = 3$ self-consistent orbitals to compute the ground state properties of the system. We also computed the following results with $M = 6$ self-consistent orbitals for convergence and checked the consistency of our results (see the supplemental material). The rotation frequency range is $\omega_r = [0, 2.5]$ for the following analysis.

We computed the ground-state energy E/N, and found it to display similar pattern as that for the elongated trap. That is for slow rotation, E/N remains almost constant and then E/N drops gradually with increase in ω_r. In addition, we found that the mean-field and many-body energies are practically identical for all ω_r. The results are shown in the supplemental material, see Fig. S1b.

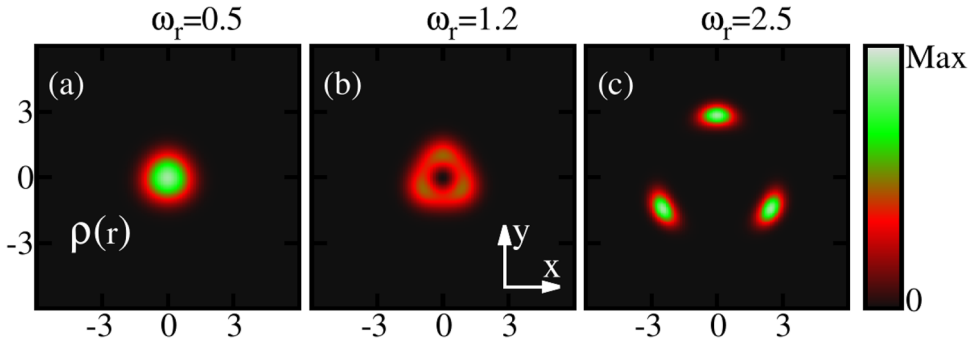

Figure 6. The one-body densities per particle are shown for three different rotation frequencies ω_r in the three-fold symmetric trap at the many-body level. M=3 self-consistent orbitals are used. The density computed at the mean-field (not shown) and many-body levels depict identical features for all ω_r. All quantities shown are dimensionless.

Figure 6 displays the ground-state densities per particle of a rotating condensate for three different rotation frequencies ω_r, confined in the three-fold symmetric trap [Eq. (19)] computed at the many-body level. In the absence of rotation, the one-body density depicts a single cloud where all the bosons accumulate in the center of the trap. However, faster rotations lead to breakup of the density profile into three clouds. We have also computed the ground state density at the mean-field level and it shows essentially identical features as the many-body level density in real space.

To further understand the breaking of the ground-state density, we discuss the behaviour of the natural occupations $\frac{n_j}{N}$ as a function of the rotation frequency ω_r as shown in Fig. 7. It is evident from Fig. 7 that the system remains fully condensed, i.e., $\frac{n_1}{N} \sim 1$, $\frac{n_2}{N} \sim \frac{n_3}{N} \sim 10^{-6}$ with the inclusion of rotation till about $\omega_r = 1.1$. From about $\omega_r = 1.2$ onwards, the condensate starts to deplete with gradual decrease in the population of the first natural orbital followed by corresponding increase in the populations of the second and third natural orbitals, $\frac{n_2}{N} \sim \frac{n_3}{N} \sim 10^{-4}$ [see Fig. S2b in the supplemental material]. For a faster rotation, say $\omega_r = 2$, the system transits to a fragmented state with decrease in the population of the first natural orbital followed by macroscopic population of the second and third natural orbitals. Further increase in the rotation to $\omega_r = 2.5$ leads to a three-fold fragmented state having the natural occupations $\frac{n_1}{N} \sim 60\%$ and $\frac{n_2}{N} \sim \frac{n_3}{N} \sim 20\%$ of the first, second, and third natural orbitals, respectively. It is observed that a perfectly three-fold fragmented state can be achievable at faster rotation in the strong interaction limit for the three-fold symmetric trap. Therefore, in case of a weakly interacting bosons confined in the three-fold symmetric trap given by Eq. (19), switching on rotation leads to a transition from a fully condensed state to three-fold fragmentation.

Let us move to the behaviour of average angular-momentum per particle $\langle \hat{L}_Z \rangle / N$, as a function of the rotation frequency ω_r for the three-fold symmetric trap computed both at the mean-field and many-body levels. It is observed from Fig. 8 that the mean-field and many-body angular momenta exactly match each other for all

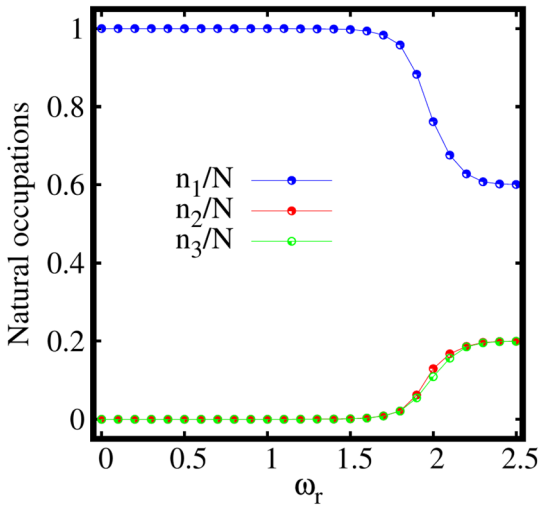

Figure 7. Pathway from condensation to fragmentation in the rotating three-fold symmetric trap. Three-fold fragmentation is observed with increase in rotation. The three leading natural occupations n_1/N, n_2/N and n_3/N, are shown as a function of the rotation frequency ω_r. $M = 3$ self-consistent orbitals are used. All quantities shown are dimensionless.

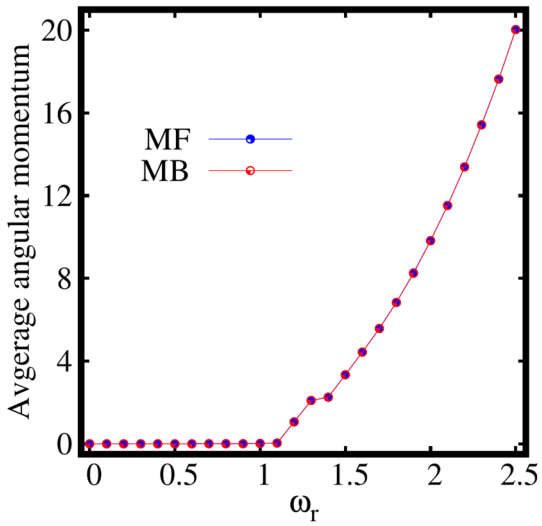

Figure 8. Expectation value of angular momentum operator $\langle \hat{L}_Z \rangle / N$, computed at the mean-field (MF) and many-body (MB) levels [with $M = 1$ and $M = 3$ self-consistent orbitals, respectively] as a function of the rotation frequency ω_r for the three-fold symmetric trap. All quantities shown are dimensionless.

ω_r. The angular momentum remains minimum till the rotation frequency of about $\omega_r = 1.1$. For about $\omega_r = 1.2$, the rotation produces a state where significant value of angular momentum generates with $\langle \hat{L}_Z \rangle / N > 1$ at which the breakup of the density is observed. The angular momentum gradually increases with further increase in the rotation of the condensate. Even for strong rotation, the angular momentum computed at the mean-field and many-body levels coincide each other. Therefore, we can conclude that, at least for the ground state, the angular momentum and its variance [see Fig. S6b in the supplemental material] are not good indicators for many-body effects. Nonetheless, we stress that the acquisition of angular momentum in the condensate follows the breakup of the density, the emergence of depletion, and the eventual fragmentation in the three-fold symmetric trap.

Now we move to the discussion of the impact of rotation on the behaviour of the many-particle variances of the position and momentum operators along the x- and y-directions, to further characterize the many-body properties of the rotating condensate undergoing breakup.

Figure 9a displays the behaviour of the many-particle position variance per particle $\frac{1}{N}\Delta^2_{\hat{X},\hat{Y}}$ as a function of the rotation frequency ω_r in the three-fold symmetric trap computed at the mean-field and many-body levels. It is observed that the mean-field and many-body $\frac{1}{N}\Delta^2_{\hat{X},\hat{Y}}$ coincide till about $\omega_r = 1.1$. For faster rotations, from about $\omega_r = 1.2$ onwards the mean-field and many-body position variances deviate. The mean-field $\frac{1}{N}\Delta^2_{\hat{X},\hat{Y}}$ increase monotonously depicting the spreading and finally the breakup of the density. However, the many-body

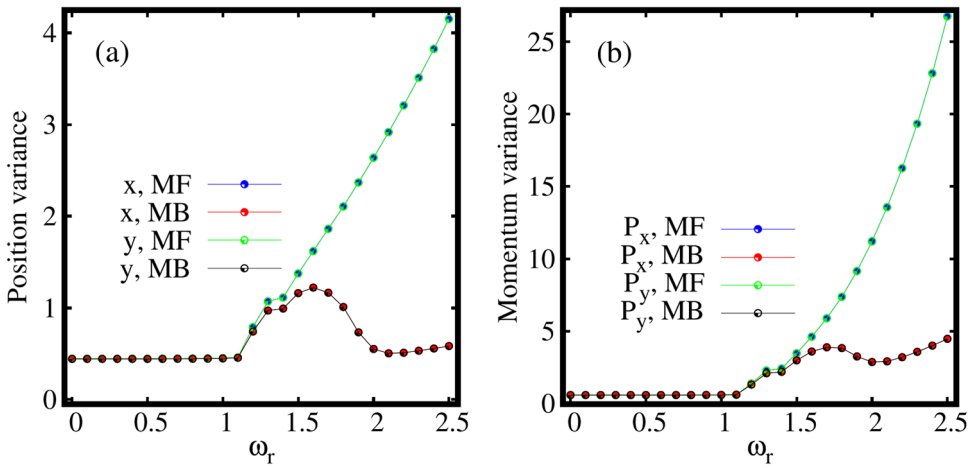

Figure 9. Dependence of the the many-particle position and momentum variances on the rotation in the three-fold symmetric trap. Shown are (**a**) $\frac{1}{N}\Delta^2_{\hat{X}}$ and $\frac{1}{N}\Delta^2_{\hat{Y}}$ and (**b**) $\frac{1}{N}\Delta^2_{\hat{P}_X}$ and $\frac{1}{N}\Delta^2_{\hat{P}_Y}$ as a function of ω_r at the many-body level (MB) [$M = 3$ self-consistent orbitals] and at the mean-field level (MF) [$M = 1$ self-consistent orbital]. All quantities shown are dimensionless.

$\frac{1}{N}\Delta^2_{\hat{X},\hat{Y}}$ first increase and then, after reaching a maximal value starts decreasing with further increase in ω_r, because of the depletion and eventual fragmentation. One of the important features of the position variance is that the variance along the x- and y-direction exactly coincide each other for both the mean-field and many-body regimes, thereby indicating the fact that the three-fold rotational symmetry of the condensate is preserved even for fast rotations. Clearly, there is no anisotropy of the variance for all ω_r in this trap.

Finally, Fig. 9b shows the behaviour of the momentum variance per particle $\frac{1}{N}\Delta^2_{\hat{P}_X,\hat{P}_Y}$, computed at the mean-field and many-body levels as a function of ω_r. The momentum variances remain small even with increase in rotation till about $\omega_r = 1.1$. From about $\omega_r = 1.2$ onwards, the momentum variances computed both at the mean-field and many-body levels slowly start to increase. Here, the mean-field momentum variance only increases monotonously. The many-body momentum variance increases, decreases, and again increases but remain much smaller than the mean-field momentum variance, indicates the presence of depletion and fragmentation. Similar to the position variance, the momentum variance along the x- and y-directions exactly coincide each other both at the mean-field and many-body levels, due to the rotational symmetry.

Bosons in a four-fold symmetric trap under rotation. Now we move to a more complicated system, a four-fold symmetric trap, to show the stability of the ground-state properties found above for the three-fold symmetric trap. The potential of the four-fold symmetric trap is given by

$$V(\mathbf{r}) = \frac{1}{4}(x^4 + y^4). \tag{20}$$

Here, we consider $M = 4$ self-consistent orbitals to obtain the ground-state properties of bosons under rotation in this trap. We also compute the results with $M = 8$ self-consistent orbitals to verify the numerical convergence, see the supplemental material. The range of rotation frequencies is taken to be $\omega_r = [0, 2.0]$ for the following study.

We computed the ground state energy E/N, and found it to display similar pattern as that for the elongated and three-fold symmetric traps. That is for slow rotation, E/N remains almost constant and then E/N drops gradually with increase in ω_r. In addition, we found that the mean-field and many-body energies are practically identical for all ω_r. The results are shown in the supplemental material, see Fig. S1c.

Figure 10 shows the behaviour of the ground-state densities per particle of a rotating BEC confined in the four-fold symmetric trap for three different rotation frequencies ω_r at the many-body level. Similar to the elongated and three-fold symmetric traps, for slow rotation the density displays a single cloud. With increasing rotation, a deep in the density emerges [Fig. 10b] and finally, faster rotations lead to splitting of the density into four sub-clouds as evident from Fig. 10c.

For a deeper understanding of the many-boson density profile, the behaviour of the natural occupations $\frac{n_j}{N}$ as a function of the rotation frequency ω_r is analyzed in Fig. 11.

It is found that the system preserves the fully condensed state, with $\frac{n_1}{N} \sim 1$, $\frac{n_2}{N} \sim \frac{n_3}{N} \sim \frac{n_4}{N} \leq 10^{-6}$, till a rotation frequency of about $\omega_r = 1.0$. Further increase in ω_r leads to slow depletion of the condensate. For a faster rotation, $\omega_r = 2.0$, four-fold fragmentation of the condensate with finite population of all the four natural orbitals is observed.

Let us discuss the behaviour of the average angular momentum per particle as a function of ω_r, see Fig. 12. The angular momentum remains minimal for $\omega_r = 1$. From about $\omega_r = 1.1$, the rotation produces a state where significant value of angular momentum generates with $\langle \hat{L}_Z \rangle / N > 1$ at which the breakup of the density is observed. The angular momentum gradually increases with further increase in the rotation. Even for strong rotation, the angular momenta computed at the mean-field and many-body levels coincide each other. Finally, it can be concluded for the four-fold trap as well that, at least for the ground state, the angular momentum and its variance [see Fig. S6c in the supplemental material] do not precisely signifies many-body effects. However, we can conclude that accumulation of angular momentum in the condensate, the breakup of the density, emergence of

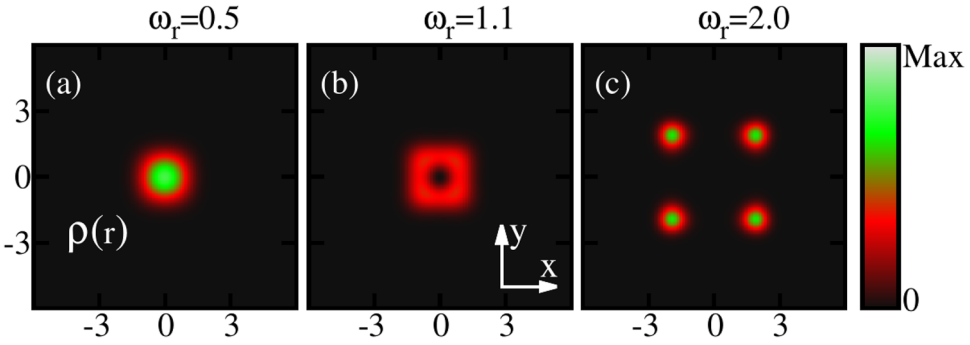

Figure 10. The one-body densities per particle are shown for three different rotation frequencies ω_r in the four-fold symmetric trap at the many-body level. M=4 self-consistent orbitals are used. The density computed at the mean-field (not shown) and many-body levels display identical features at all ω_r. All quantities shown are dimensionless.

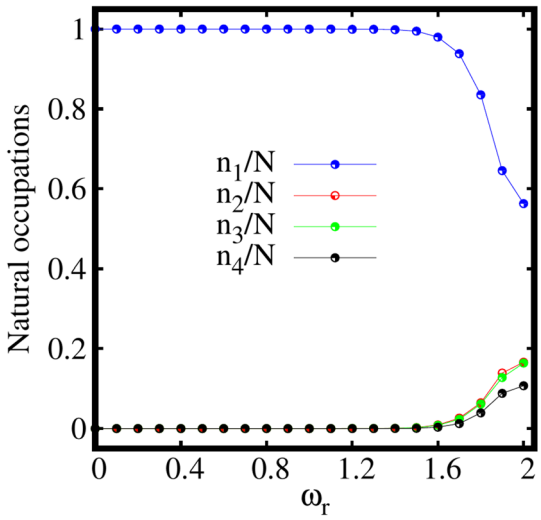

Figure 11. Rotation leads to four-fold fragmentation in the four-fold symmetric trap. $M = 4$ self-consistent orbitals are used. The variation of four natural occupations n_1/N, n_2/N, n_3/N and n_4/N are shown as a function of rotation frequency ω_r. All quantities computed are dimensionless.

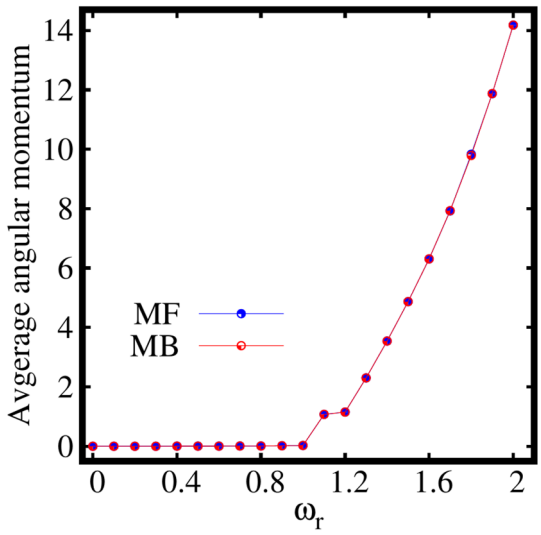

Figure 12. Expectation value of angular momentum operator $\langle \hat{L}_Z \rangle / N$, computed at the mean-field (MF) and many-body (MB) levels [with $M = 1$ and $M = 4$ self-consistent orbitals, respectively] as a function of the rotation frequency ω_r for the four-fold symmetric trap. All quantities shown are dimensionless.

depletion, and eventual fragmentation in the four-fold symmetric trap are in sync similar to the elongated and three-fold symmetric traps.

Figure 13 displays the behaviour of the position and momentum variances computed at the mean-field and many-body levels as a function of rotation frequency ω_r for four-fold symmetric trap along the x- and y-directions. The mean-field and many-body position variances $\frac{1}{N}\Delta^2_{\hat{X},\hat{Y}}$ coincide till about $\omega_r = 1$. For faster rotations, from about $\omega_r = 1.1$ onward, the mean-field position variance deviates from the many-body position variance and the former is always larger than the latter. Further, the position variances along the x- and y-directions exactly coincide with each other both at the mean-field and many-body levels similar to the three-fold symmetric trap, see Fig. 9a. Side by side, the behaviour of the momentum variance $\frac{1}{N}\Delta^2_{\hat{P}_X,\hat{P}_Y}$ displays similar feature as that of the position variance, both at the mean-field and many-body levels. In particular, mean-field is larger than many-body from about $\omega_r = 1.5$.

Finally, we can conclude that the depletion, angular momentum, and the position and momentum variances follow hand in hand both in the three-fold and four-fold symmetric traps. The rotating interacting bosons acquire unique many-body properties while undergoing breakup in space.

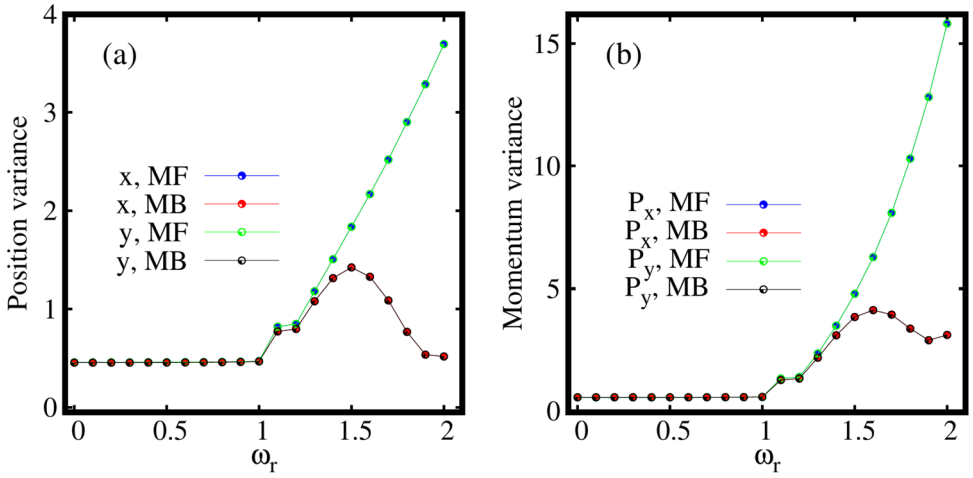

Figure 13. Dependence of the the many-particle position and momentum variances on the rotation in the four-fold symmetric trap. (**a**) depicts the position variances $\frac{1}{N}\Delta^2_{\hat{X}}$, $\frac{1}{N}\Delta^2_{\hat{Y}}$ and (**b**) displays momentum variances $\frac{1}{N}\Delta^2_{\hat{P}_X}$, $\frac{1}{N}\Delta^2_{\hat{P}_Y}$ at the many-body level (MB) [$M = 4$ self-consistent orbitals] and at the mean-field level (MF) [$M = 1$ self-consistent orbital]. All quantities shown are dimensionless.

Concluding remarks

In the present work, we have studied the impact of rotation on the ground state of weakly interacting bosonic atoms confined in two-dimensional anharmonic potentials, first in, an elongated trap and, subsequently, in three-fold and four-fold symmetric traps. Here, the multiconfigurational time-dependent Hartree method for bosons, which is particularly suitable to describe many-body properties, is employed to investigate the ground-state energy, density, the depletion and fragmentation, angular momentum, and finally, many-particle variances as a function of the rotation frequency to characterize the correlations present in the system.

In the elongated trap, it is observed that the ground-state density breaks up into two clouds with rotation. The splitting of the density is followed by the emergence of the two-fold fragmentation. Interestingly, the ground state exhibits opposite anistoropy both for the many-particle position and momentum variances when computed at the many-body and mean-field levels. The rotation squeezes the position variance in the elongated direction and the momentum variance in the narrow direction, thereby producing unique correlations. Finally, a synchronized pattern among the density breakup, eventual fragmentation, acquisition of angular momentum in the condensate, and many-particle variances is observed. When the angular momentum sets in the breakup of density and the many-particle position and momentum variances start to increase.

For the three-fold and four-fold symmetric traps, the ground-state density eventually splits into three and four clouds, respectively, with the inclusion of the rotation. Side-by-side, the rotation leads to transition from condensed to three-fold and four-fold fragmented condensates, respectively, at the many-body level of theory. We find that the depletion, the accumulation of angular momentum, and finally, the increase in the variances of position and momentum follow hand in hand.

The rotating frame in our work can be viewed as a specific case of synthetic gauge fields. In future, continuation of this investigation includes the extension of the study in various synthetic gauge fields. It would be interesting to explore the ground-state breakup, eventual condensation or fragmentation, and finally, various correlations of the condensate in presence of synthetic gauge fields. It would be fascinating to discover many-body features beyond the capacity of a "simple" rotation.

Data availability

The datasets generated during and/or analyzed during the current study are available from the corresponding author on reasonable request.

Received: 28 October 2022; Accepted: 6 February 2023
Published online: 27 February 2023

References

1. Madison, K. W., Chevy, F., Wohlleben, W. & Dalibard, J. Vortex formation in a stirred Bose–Einstein condensate. *Phys. Rev. Lett.* **84**, 806 (2000).
2. Raman, C., Abo-Shaeer, J., Vogels, J., Xu, K. & Ketterle, W. Vortex nucleation in a stirred Bose–Einstein condensate. *Phys. Rev. Lett.* **87**, 210402 (2001).
3. Matthews, M. R. *et al.* Vortices in a Bose–Einstein condensate. *Phys. Rev. Lett.* **83**, 2498 (1999).
4. Haljan, P., Anderson, B., Coddington, I. & Cornell, E. A. Use of surface-wave spectroscopy to characterize tilt modes of a vortex in a Bose–Einstein condensate. *Phys. Rev. Lett.* **86**, 2922 (2001).
5. Abo-Shaeer, J., Raman, C. & Ketterle, W. Formation and decay of vortex lattices in Bose–Einstein condensates at finite temperatures. *Phys. Rev. Lett.* **88**, 070409 (2002).

6. Butts, D. & Rokhsar, D. Predicted signatures of rotating Bose–Einstein condensates. *Nature* **397**, 327–329 (1999).
7. Dagnino, D., Barberán, N., Lewenstein, M. & Dalibard, J. Vortex nucleation as a case study of symmetry breaking in quantum systems. *Nat. Phys.* **5**, 431–437 (2009).
8. Coddington, I., Engels, P., Schweikhard, V. & Cornell, E. A. Observation of Tkachenko oscillations in rapidly rotating Bose–Einstein condensates. *Phys. Rev. Lett.* **91**, 100402 (2003).
9. Schweikhard, V., Coddington, I., Engels, P., Mogendorff, V. P. & Cornell, E. A. Rapidly rotating Bose–Einstein condensates in and near the lowest Landau level. *Phys. Rev. Lett.* **92**, 040404 (2004).
10. Regnault, N. & Jolicoeur, T. Quantum hall fractions in rotating Bose–Einstein condensates. *Phys. Rev. Lett.* **91**, 030402 (2003).
11. Chiappini, C. *et al.* Imprints of fast-rotating massive stars in the galactic bulge. *Nature* **472**, 454–457 (2011).
12. Bohr, A. & Mottelson, B. R. Physics of rapidly rotating nuclei. *Phys. Today* **32**, 25–31 (1979).
13. Guo, Y. *et al.* Supersonic rotation of a superfluid: A long-lived dynamical ring. *Phys. Rev. Lett.* **124**, 025301 (2020).
14. Kumar, R. K., Sriraman, T., Fabrelli, H., Muruganandam, P. & Gammal, A. Three-dimensional vortex structures in a rotating dipolar Bose–Einstein condensate. *J. Phys. B: At. Mol. Opt. Phys.* **49**, 155301 (2016).
15. Brito, L., Andriati, A., Tomio, L. & Gammal, A. Breakup of rotating asymmetric quartic-quadratic trapped condensates. *Phys. Rev. A* **102**, 063330 (2020).
16. Aftalion, A. *Vortices in Bose–Einstein condensates* Vol. 67 (Springer Science & Business Media, Heidelberg, 2007).
17. Fetter, A. L. Rotating trapped Bose–Einstein condensates. *Rev. Mod. Phys.* **81**, 647 (2009).
18. Tsatsos, M. C. *et al.* Quantum turbulence in trapped atomic Bose–Einstein condensates. *Phys. Rep.* **622**, 1–52 (2016).
19. Viefers, S., Hansson, T. & Reimann, S. Bose condensates at high angular momenta. *Phys. Rev. A* **62**, 053604 (2000).
20. Reimann, S., Koskinen, M., Yu, Y. & Manninen, M. Rotating quantum liquids crystallize. *New J. Phys.* **8**, 59 (2006).
21. Cremon, J., Kavoulakis, G., Mottelson, B. & Reimann, S. Vortices in Bose–Einstein condensates: Finite-size effects and the thermodynamic limit. *Phys. Rev. A* **87**, 053615 (2013).
22. Cremon, J. *et al.* Rotating Bose–Einstein condensates: Closing the gap between exact and mean-field solutions. *Phys. Rev. A* **91**, 033623 (2015).
23. Beinke, R., Cederbaum, L. S. & Alon, O. E. Enhanced many-body effects in the excitation spectrum of a weakly interacting rotating Bose–Einstein condensate. *Phys. Rev. A* **98**, 053634 (2018).
24. Khanore, M. P. & Dey, B. The quantum vortex states in extended Bose-Hubbard model: effects of lattice geometries, inter-particle interactions and spatial inhomogeneity. *Eur. Phys. J. D* **76**, 1–13 (2022).
25. Löwdin, P.-O. Quantum theory of many-particle systems. I. physical interpretations by means of density matrices, natural spin-orbitals, and convergence problems in the method of configurational interaction. *Phys. Rev.* **97**, 1474 (1955).
26. Yang, C. N. Concept of off-diagonal long-range order and the quantum phases of liquid He and of superconductors. *Rev. Mod. Phys.* **34**, 694 (1962).
27. Davidson, E. *Reduced density matrices in quantum chemistry* Vol. 6 (Academic Press, New York, 1976).
28. Coleman, A. J. & Yukalov, V. I. *Reduced density matrices: Coulson's challenge* Vol. 72 (Lectures Notes in Chemistry; Springer, Berlin, 2000).
29. Fischer, U. R., Lode, A. U. & Chatterjee, B. Condensate fragmentation as a sensitive measure of the quantum many-body behavior of bosons with long-range interactions. *Phys. Rev. A* **91**, 063621 (2015).
30. Lode, A. U. Multiconfigurational time-dependent Hartree method for bosons with internal degrees of freedom: Theory and composite fragmentation of multicomponent Bose–Einstein condensates. *Phys. Rev. A* **93**, 063601 (2016).
31. Penrose, O. & Onsager, L. Bose–Einstein condensation and liquid Helium. *Phys. Rev.* **104**, 576 (1956).
32. Mueller, E. J., Ho, T.-L., Ueda, M. & Baym, G. Fragmentation of Bose–Einstein condensates. *Phys. Rev. A* **74**, 033612 (2006).
33. Girardeau, M. Simple and generalized condensation in many-Boson systems. *Phys. Fluids* **5**, 1468–1478 (1962).
34. Spekkens, R. & Sipe, J. Spatial fragmentation of a Bose–Einstein condensate in a double-well potential. *Phys. Rev. A* **59**, 3868 (1999).
35. Streltsov, A. I., Cederbaum, L. S. & Moiseyev, N. Ground-state fragmentation of repulsive Bose–Einstein condensates in double-trap potentials. *Phys. Rev. A* **70**, 053607 (2004).
36. Streltsov, A. I. & Cederbaum, L. S. Properties of fragmented repulsive condensates. *Phys. Rev. A* **71**, 063612 (2005).
37. Alon, O. E. & Cederbaum, L. S. Pathway from condensation via fragmentation to fermionization of cold bosonic systems. *Phys. Rev. Lett.* **95**, 140402 (2005).
38. Bader, P. & Fischer, U. R. Fragmented many-body ground states for scalar bosons in a single trap. *Phys. Rev. Lett.* **103**, 060402 (2009).
39. Fischer, U. R. & Bader, P. Interacting trapped bosons yield fragmented condensate states in low dimensions. *Phys. Rev. A* **82**, 013607 (2010).
40. Zhou, Q. & Cui, X. Fate of a Bose–Einstein condensate in the presence of spin-orbit coupling. *Phys. Rev. Lett.* **110**, 140407 (2013).
41. Kawaguchi, Y. Goldstone-mode instability leading to fragmentation in a spinor Bose–Einstein condensate. *Phys. Rev. A* **89**, 033627 (2014).
42. Song, S.-W., Zhang, Y.-C., Zhao, H., Wang, X. & Liu, W.-M. Fragmentation of spin-orbit-coupled spinor Bose–Einstein condensates. *Phys. Rev. A* **89**, 063613 (2014).
43. Kang, M.-K. & Fischer, U. R. Revealing single-trap condensate fragmentation by measuring density-density correlations after time of flight. *Phys. Rev. Lett.* **113**, 140404 (2014).
44. Jen, H.-H. & Yip, S.-K. Fragmented many-body states of a spin-2 bose gas. *Phys. Rev. A* **91**, 063603 (2015).
45. Fischer, U. R. & Kang, M.-K. "Photonic" cat states from strongly interacting matter waves. *Phys. Rev. Lett.* **115**, 260404 (2015).
46. Kolovsky, A. R. Bogoliubov depletion of the fragmented condensate in the bosonic flux ladder. *Phys. Rev. A* **95**, 033622 (2017).
47. Tomchenko, M. On a fragmented condensate in a uniform bose system. *J. Low Temp. Phys.* **198**, 100–121 (2020).
48. Sakmann, K. & Kasevich, M. Single-shot simulations of dynamic quantum many-body systems. *Nat. Phys.* **12**, 451 (2016).
49. Fletcher, R. J. *et al.* Geometric squeezing into the lowest landau level. *Science* **372**, 1318–1322 (2021).
50. Mukherjee, B. *et al.* Crystallization of bosonic quantum hall states in a rotating quantum gas. *Nature* **601**, 58–62 (2022).
51. Sánchez-Lotero, P. & Palacios, J. J. Vortices in a rotating Bose–Einstein condensate under extreme elongation. *Phys. Rev. A* **72**, 043613 (2005).
52. Williams, J. & Holland, M. Preparing topological states of a Bose–Einstein condensate. *Nature (London)* **401**, 568–572 (1999).
53. Beinke, R., Klaiman, S., Cederbaum, L. S., Streltsov, A. I. & Alon, O. E. Many-body tunneling dynamics of Bose–Einstein condensates and vortex states in two spatial dimensions. *Phys. Rev. A* **92**, 043627 (2015).
54. Alon, O. E. Analysis of a trapped Bose–Einstein condensate in terms of position, momentum, and angular-momentum variance. *Symmetry* **11**, 1344 (2019).
55. Gross, E. P. Structure of a quantized vortex in boson systems. *Il Nuovo Cimento* **20**, 454–477 (1961).
56. Pitaevskii, L. P. Vortex lines in an imperfect Bose gas. *Sov. Phys. JETP* **13**, 451–454 (1961).
57. Streltsov, A. I., Alon, O. E. & Cederbaum, L. S. Role of excited states in the splitting of a trapped interacting Bose–Einstein condensate by a time-dependent barrier. *Phys. Rev. Lett.* **99**, 030402 (2007).
58. Alon, O. E., Streltsov, A. I. & Cederbaum, L. S. Multiconfigurational time-dependent Hartree method for bosons: Many-body dynamics of bosonic systems. *Phys. Rev. A* **77**, 033613 (2008).
59. Beck, M. H., Jäckle, A., Worth, G. A. & Meyer, H. D. The multiconfiguration time-dependent Hartree (MCTDH) method: A highly efficient algorithm for propagating wavepackets. *Phys. Rep.* **324**, 1–105 (2000).

60. Wang, H. & Thoss, M. Multilayer formulation of the multiconfiguration time-dependent Hartree theory. *J. Chem. Phys.* **119**, 1289 (2003).
61. Manthe, U. A multilayer multiconfigurational time-dependent Hartree approach for quantum dynamics on general potential energy surfaces. *J. Chem. Phys.* **128**, 164116 (2008).
62. Wang, H. Multilayer multiconfiguration time-dependent Hartree theory. *J. Phys. Chem. A* **119**, 7951–7965 (2015).
63. Manthe, U. & Weike, T. On the multi-layer multi-configurational time-dependent Hartree approach for bosons and fermions. *J. Chem. Phys.* **146**, 064117 (2017).
64. Manthe, U. Wavepacket dynamics and the multi-configurational time-dependent Hartree approach. *J. Phys.: Condens. Matter* **29**, 253001 (2017).
65. Bhowmik, A., Haldar, S. K. & Alon, O. E. Impact of the transverse direction on the many-body tunneling dynamics in a two-dimensional bosonic Josephson junction. *Sci. Rep.* **10**, 21476 (2020).
66. Bhowmik, A. & Alon, O. E. Longitudinal and transversal resonant tunneling of interacting bosons in a two-dimensional Josephson junction. *Sci. Rep.* **12**, 627 (2022).
67. Zanghellini, J., Kitzler, M., Fabian, C., Brabec, T. & Scrinzi, A. An MCTDHF approach to multielectron dynamics in laser fields. *Laser Phys.* **13**, 1064 (2003).
68. Cao, L., Krönke, S., Vendrell, O. & Schmelcher, P. The multi-layer multi-configuration time-dependent Hartree method for bosons: Theory, implementation, and applications. *J. Chem. Phys.* **139**, 134103 (2013).
69. Cao, L. *et al.* A unified ab initio approach to the correlated quantum dynamics of ultracold fermionic and bosonic mixtures. *J. Chem. Phys.* **147**, 044106 (2017).
70. Haxton, D. J. & McCurdy, C. W. Two methods for restricted configuration spaces within the multiconfiguration time-dependent Hartree-Fock method. *Phys. Rev. A* **91**, 012509 (2015).
71. Miyagi, H. & Madsen, L. B. Time-dependent restricted-active-space self-consistent-field theory with space partition. *Phys. Rev. A* **95**, 023415 (2017).
72. Lévêque, C. & Madsen, L. B. Time-dependent restricted-active-space self-consistent-field theory for bosonic many-body systems. *New J. Phys.* **19**, 043007 (2017).
73. Lévêque, C. & Madsen, L. B. Multispecies time-dependent restricted-active-space self-consistent-field theory for ultracold atomic and molecular gases. *J. Phys. B: At. Mol. Opt. Phys.* **51**, 155302 (2018).
74. Lode, A. U. J., Lévêque, C., Madsen, L. B., Streltsov, A. I. & Alon, O. E. Colloquium : Multiconfigurational time-dependent Hartree approaches for indistinguishable particles. *Rev. Mod. Phys.* **92**, 011001 (2020).
75. Lode, A. U. J. *et al.* MCTDH-X: The time-dependent multiconfigurational Hartree for indistinguishable particles software (2019).
76. Lin, R. *et al.* MCTDH-X: The multiconfigurational time-dependent Hartree method for indistinguishable particles software. *Quantum Sci. Technol.* **5**, 024004 (2020).
77. Lode, A. U. J. *et al.* MCTDH-X: The multiconfigurational time-dependent Hartree method for indistinguishable particles high-performance computation project. In *High Performance Computing in Science and Engineering'20*, pp. 21–45 (Springer, 2021).
78. Lode, A. U., Sakmann, K., Alon, O. E., Cederbaum, L. S. & Streltsov, A. I. Numerically exact quantum dynamics of bosons with time-dependent interactions of harmonic type. *Phys. Rev. A* **86**, 063606 (2012).
79. Doganov, R. A., Klaiman, S., Alon, O. E., Streltsov, A. I. & Cederbaum, L. S. Two trapped particles interacting by a finite-range two-body potential in two spatial dimensions. *Phys. Rev. A* **87**, 033631 (2013).
80. Dirac, P. A. M. Note on exchange phenomena in the Thomas Atom. *Math. Proc. Cambridge Philos. Soc.* **26**, 376 (1930).
81. Mott, N. F. & Frenkel, J. *Wave Mechanics: Advanced General Theory* Vol. 18 (Clarendon Press, Oxford, 1934).
82. Kramer, P. & Saraceno, M. *Geometry of the time-dependent variational principle in quantum mechanics* (Springer, Notes in Physics, London, 2007).
83. Weiner, S. E., Tsatsos, M. C., Cederbaum, L. S. & Lode, A. U. Phantom vortices: Hidden angular momentum in ultracold dilute Bose–Einstein condensates. *Sci. Rep.* **7**, 40122 (2017).
84. Tsatsos, M. C., Streltsov, A. I., Alon, O. E. & Cederbaum, L. S. Fragmented many-body states of definite angular momentum and stability of attractive three-dimensional condensates. *Phys. Rev. A* **82**, 33613 (2010).
85. Klaiman, S. & Alon, O. E. Variance as a sensitive probe of correlations. *Phys. Rev. A* **91**, 063613 (2015).
86. Alon, O. E. Variance of a trapped Bose–Einstein condensate. *J. Phys: Conf. Ser.* **1206**, 012009 (2019).

Acknowledgements

This work is supported by the Israel Science Foundation (ISF) grant no. 1516/19 and by the Austrian Science Foundation (FWF) under grant P-32033-N32. SD acknowledges Anal Bhowmik for helpful discussions. Computation time at the High-Performance Computing Center Stuttgart (HLRS) is gratefully acknowledged.

Author contributions

S.D. and O.E.A. conceived the problem. S.D. performed the research and calculations. S.D., A.U.J.L., and O.E.A. wrote the paper.

Competing interests

The authors declare no competing interests.

Additional information

Supplementary Information The online version contains supplementary material available at https://doi.org/10.1038/s41598-023-29516-w.

Correspondence and requests for materials should be addressed to S.D.